Design of Dual-Mode Stimulus Chip With Built-In High Voltage Generator for Biomedical Applications

Ting-Yang Yen and Ming-Dou Ker, *Fellow, IEEE*

***Abstract*—In this work, a dual-mode stimulus chip with a built-in high voltage generator was proposed to offer a broad-range current or voltage stimulus patterns for biomedical applications. With an on-chip and built-in high voltage generator, this stimulus chip could generate the required high voltage supply without additional supply voltage. With a nearly 20 V operating voltage, the over-stress and reliability issues of the stimulus circuits were thoroughly considered and carefully addressed in this work. This stimulus system only requires an area of 0.22 mm^2 per single channel and is fully on-chip implemented without any additional external components. The dual-mode stimulus chip was fabricated in a 0.25-μm 2.5V/5V/12V CMOS (complementary metal-oxide-semiconductor) process, which can generate the biphasic current or voltage stimulus pulses. The current level of stimulus is up to 5 mA, and the voltage level of stimulus can be up to 10 V. Moreover, this chip has been successfully applied to stimulate a guinea pig in an animal experiment. The proposed dual-mode stimulus system has been verified in electrical tests and also demonstrated its stimulation function in animal experiments.**

***Index Terms*—Biphasic stimulus, charge pump circuit, constant current mode (CCM) stimulation, constant voltage mode (CVM) stimulation, dual-mode stimulus, high voltage generator.**

I. Introduction

Although modern medical technology has been quite advanced, there are still some neurological disorders those cannot be cured with even known methods. Attempts to curb the progression of some of diseases include pharmacological treatments or surgery. However, the solutions suffered some limitations. For instance, some patients are allergic to specific medicines. The surgical treatment would not be performed in some particular cases, if the abnormal region is a controlled physiological region of the brain. Fortunately, the well-developed microelectronic technologies have become instrumental to the medical applications. For instance, electrical stimulators, such as cochlear implants to treat hearing damage [1], deep brain stimulators [2]–[5], spinal cord stimulations for the restoration of motor functions [6], [7], applications for retinal implants [8]–[10], seizure suppression techniques [11]–[13], artificial pacemakers, and those used for other biomedical applications [14], [15], have been widely used in the medical field. Among these applications, stimulations are sometimes used to suppress abnormal nerve potentials and to trigger a nervous response. Stimulators are crucial in delivering stimulus signals to receptors. A typical implantable stimulator system on chip (SoC) is shown in Fig. 1. The whole SoC is powered by the power management unit (PMU), such as the rectifier and regulator, and the power source of the PMU is transmitted wirelessly through an external chip. The bio-signal processor always monitors the nerve potential. Once the potential of the neural signal is higher than the threshold potential set in the bio-signal processor, the processor will deliver the control signal to the stimulus system that in turn send out the desired stimulus current or voltage pattern to the biological tissue.

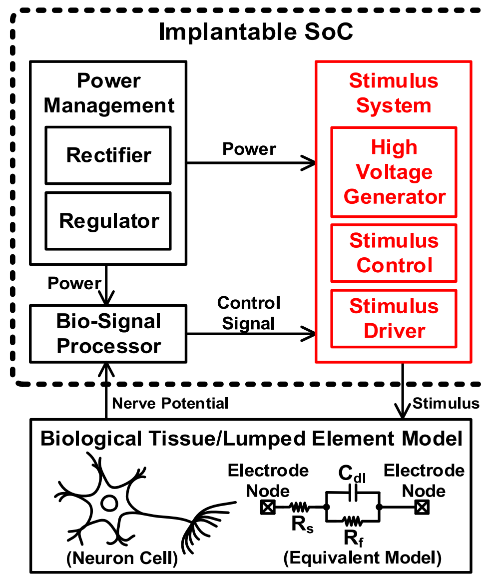

Fig. 1. Block diagram of implantable system on chip (SoC) for biomedical applications and tissue (neuron cell) with its equivalent impedance network.

The biological tissue can be modeled as a lump circuit network, which includes a solution resistor R_s, a faradaic resistance R_f, and a double-layer capacitance C_{dl} [16]. Unfortunately, the value of components is nonstationary due to the application fields of stimulators, the type of electrode, the location and distance of sticking to biological tissues, and even the implantation time of the electronic device [17], [18]. For example, the C_{dl}, R_f, and R_s are found as 500 nF, 10 MΩ, and 4 kΩ, respectively,

Manuscript received March 14, 2020; revised May 5, 2020; accepted May 27, 2020. Date of publication June 2, 2020; date of current version October 15, 2020. This work was supported in part by the Ministry of Education (MOE) through the SPROUT Project – Center for Neuromodulation Medical Electronics Systems of National Chiao Tung University, Taiwan, and in part by the Ministry of Science and Technology (MOST), Taiwan under Contract 108-2321-B-009-007-MY2. The fabrication of silicon chip is supported by Taiwan Semiconductor Research Institute (TSRI). *(Corresponding author: Ming-Dou Ker.)*

The authors are with the Institute of Electronics, National Chiao Tung University, Hsinchu 300, Taiwan (e-mail: e179981314@gmail.com; mdker@ieee.org).

Color versions of one or more of the figures in this article are available online at https://ieeexplore.ieee.org.

Digital Object Identifier 10.1109/TBCAS.2020.2999398

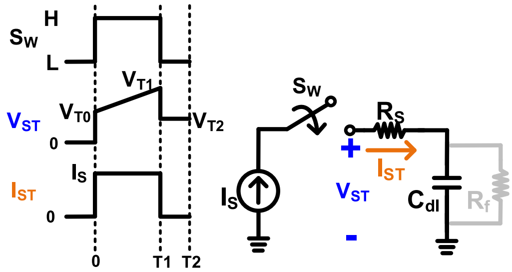

(a)

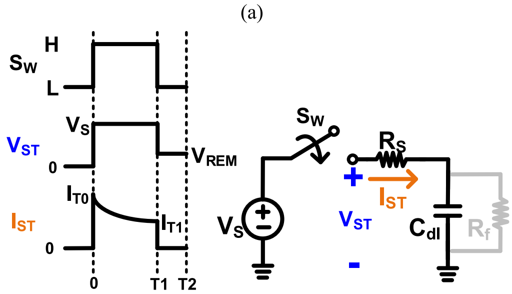

(b)

Fig. 2. Stimulators designed with (a) constant current mode (CCM) and (b) constant voltage mode (CVM).

in the seizure suppression applications [19]. But, another case showed that the range of R_s is 24 $\sim$ 200 kΩ and C_{dl} is 1 μF [20].

There are implementation tradeoffs in the stimulator design, including the mode of stimulation, electrode configuration, and the stimulus pattern. In this work, the bipolar (H-bridge) electrode configuration is used with the design and operation of the corresponding circuit. When a complete stimulation phase is needed, two sets of driver circuits are co-operated to perform the desired biphasic stimulus current or voltage pulse. For the other unselected drivers, their switches are fully turned off to avoid unnecessary stimulations in the inactive channels. Moreover, the biphasic stimulus pattern is applied with the consideration of charge balance. There are two main stimulation modes in this stimulator design, including the constant current mode (CCM) and the constant voltage mode (CVM). The circuit topology and corresponding waveforms of these two modes are depicted in Figs. 2(a) and (b), respectively. As aforementioned, the R_f is usually with a higher value of mega-ohm, so its effect can be almost negligible in this lumped model. Therefore, the model can be further simplified into the form of one resistor (R_s) in series with one capacitance (C_{dl}). If the stimulus current I_{ST} is constant, the charge injected into the tissue during the T_1 period will be $I_{\mathrm{ST}} \times T_1$. Delivering an identical reverse current pulse at a later time period is the simplest way to achieve the charge balance in the CCM operation. Even with the same amplitude and biphasic pulse, the charge balance is somewhat challenging to be accomplished in the CVM operation. The charge injected in the first pulse of CVM will be remained on C_{dl} to cause the residual voltage $V_{\mathrm{REM,}}$ as shown in Fig. 2(b), which will seriously affect the stimulus current (charge injected) caused by the next pulse.

Some studies on the accuracy and improvement of the charge balance techniques in the CCM had been reported [21]–[23]. However, fewer studies were done in the CVM. Calculating or measuring the residual charge to achieve charge balance in the CVM is necessary [24]. Due to the therapeutic effects of stimulation and the charge features for safety, the CCM has been widely adopted for most stimulators. There are also some other current stimulation patterns those are implemented in the current mode [25]. However, the CCM requires a higher supply voltage than the CVM under the same stimulus current level. For a rectangular current pulse, the minimum supply voltage for the CCM can be calculated as

$$\mathrm{VDD_{MIN}} = V_H + (I_{ST} \times R_S) + \frac{I_{ST} \times T_1}{C_{dl}} \tag{1}$$

where V_H represents the minimum voltage headroom for the circuit of current source, the second term $I_{\mathrm{ST}} \times R_S$ can be understood as V_{T0}, and the last term is the voltage difference between V_{T1} and V_{T0} due to the charging of C_{dl} which has been depicted in Fig. 2(a). For instance, if the given I_{ST}, C_{dl}, and T_1 are 3 mA, 10 nF, and 50 μs, respectively, this condition will produce a voltage difference of up to 15 V during the T_1 period. In other words, the minimum supply voltage required by the CCM may often exceed the general chip specifications. As comparing to the CCM, the $\mathrm{VDD_{MIN}}$ in the CVM operation only requires 9 V to generate a stimulus current of 3 mA onto the Rs of 3 kΩ. The power efficiency in the CCM is worse than that in the CVM [26], [27]. Although some works had proposed to adjust their supply voltages dynamically [28], [29], those proposed methods still need to satisfy the Equation (1).

Furthermore, in practical medical applications, the CVM was still efficacious and necessary for some patients [30]. Therefore, some CVM stimulators were reported. In addition, there are some stimulator works implemented with the technique of switching mode power supply (SMPS), which required huge external components, such as inductances, thereby increasing the difficulty for implantable applications [31], [32]. In summary, the CCM and CVM have different electrical characteristics and loading ranges in stimulus operations. If these two modes in stimulus operations can be combined, the stimulator system will become more comprehensive.

In this work, a dual-mode stimulus system was proposed, which can output 5 mA in CCM or 10 V in the CVM under the given load conditions. For example, R_s is in the range of several kilo-ohm, C_{dl} is in the range of nano-farad, and R_f is in the range of the mega-ohm. Adapting to such an impedance range in biomedical applications, the specifications of CCM and CVM stimulations were designed at 5 mA and 10 V, respectively. In addition, considering such loading conditions and stimulus amplitudes, a supply voltage up to a range of 10 V$\sim$20 V will be needed. The standard supply voltage (2.5 V and 5 V) in a microelectronics system is not enough, so a built-in charge pump (CP) was also implemented in the stimulus chip together. This stimulus system can be implemented fully on-chip without any external components, which is quite suitable for implantable SoC with multi-channel applications.

The paper is organized as follows. Section II explains the details of the dual-mode operation. Section III demonstrates the measurement results in silicon, the animal experiment results,

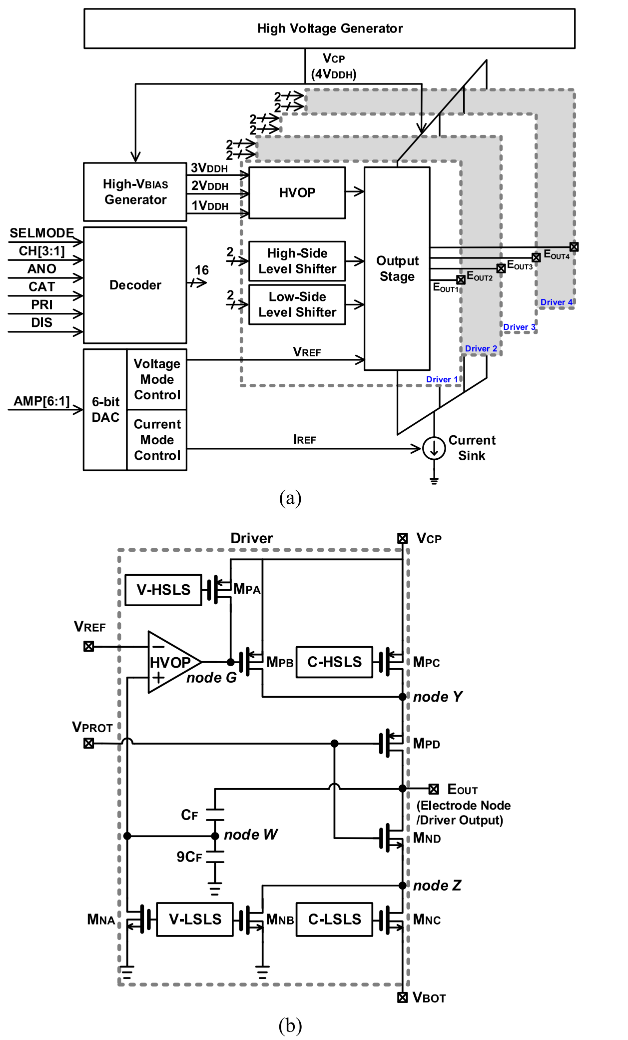

Fig. 3. (a) Block diagram of the dual-mode stimulus system. (b) Transistor-level schematic of a single driver (channel) circuit.

and some biomedical applications. Finally, Section IV is the conclusion.

II. Proposed Dual-Mode Stimulus Circuit

A dual-mode stimulus system was designed to generate either current or voltage stimulus pulses, which can deliver the stimulus current of several milli-amps or the stimulus voltage of several volts. A built-in high voltage generator was implemented by the charge pump circuit to support the broad power requirement. Due to the high voltage operation, reliability and overstress issues were carefully considered in this work.

A. Overall Architecture

The proposed stimulus system is composed of a high voltage-bias (V_{BIAS}) generator, a decoder, a 6-bit digital-to-analog circuit (DAC), the CCM and CVM control circuit, a current sink, a 4-channel driver, and a high voltage generator, as demonstrated in Fig. 3(a). Since the proposed stimulator works under $4\mathrm{V}_{\mathrm{DDH}}$, the power voltage ($V_{\mathrm{CP}}$) is supplied by the charge pump. The decoder is in charge of selecting stimulus modes, stimulus levels, and stimulus sequences. In each driver circuit, the decoder gives control signals through level shifters to drive the output stage. The high-side level shifter (HSLS) and low-side level shifter (LSLS) can transfer the control signals to a proper power domain. With the high voltage operational amplifier (HVOP), the driver can produce a precise, steady, and constant stimulus pulse. As shown in Fig. 3(b), the operation of a driver is sorted into the CCM or CVM operation by a switch (M_{PA}). The current-mode high-side level shifter (C-HSLS) and low-side level shifter (C-LSLS) pass the corresponding signals for the primary switches (M_{PC} and M_{NC}) in the CCM operation. In the CVM operation, the driving switches (M_{PB} and M_{NB}) are controlled by other voltage-mode level shifters (V-HSLS and V-LSLS). M_{PA} and M_{NA} in Fig. 3(b) are mainly used to reset the driver and biological tissue. Moreover, the 6-bit DAC provides the reference voltage for CVM operation or an accurate current source for CCM operation. Thus, the proposed stimulus system can offer constant stimulation under the selected modes. Furthermore, the 6-bit DAC was adopted as the thermometer type to achieve a decreased number of switching current glitches. The ramp pattern of the stimulus pulses is beneficial for some biomedical applications.

B. Dual-Mode Stimulus: Current Mode Operation

Fig. 4 shows the complete operation and control sequences in the CCM operation. There are four operation phases, including the cathodic stimulus (C), inter-delay (I), anodic stimulus (A), and discharge (D) phases. In the CCM, HVOP is disabled while the current sink is enabled. The current sink can adjust the current stimulus levels. Initially, most of the transistors stay off except M_{PA1} and M_{PA2}.

As shown in Fig. 4, the driver 2 delivers a current stimulus pulse to the driver 1 as a cathodic stimulus current (I_{CAT}) on the biological tissue. In the cathodic stimulus phase, M_{PA1} and M_{PA2} are also turned on, so that the voltage at nodes G1 and G2 will be charged to $4\mathrm{V}_{\mathrm{DDH}}$. M_{PB1} and M_{PB2}, which used in the voltage stimulus mode, are turned off to prevent the unnecessary current path. After the control signals pass through C2-HSLS and C1-LSLS, the gates of M_{PC2} and M_{NC1} are biased at $3\mathrm{V}_{\mathrm{DDH}}$ (15 V) and $1\mathrm{V}_{\mathrm{DDH}}$ (5 V), respectively. The current sink can draw charges from power node V_{CP} and compose the cathodic stimulus path (shown with the red line). The cathodic current sequentially flows through M_{PC2}, M_{PD2}, E_{OUT2} (one of the electrode nodes), biological tissue, E_{OUT1} (another electrode node), $M_{\mathrm{ND1,}}$ and M_{NC1}.

During stimulation, the E_{OUT} nodes might be raised to some voltage levels between 0 and $4\mathrm{V}_{\mathrm{DDH}}$ (20V). Since the 12-V devices used in the circuit is with $2\mathrm{V}_{\mathrm{DDH}}$ tolerance in the given process, the voltage limiting technique was applied. V_{PROT} was designed to bias at $2\mathrm{V}_{\mathrm{DDH}}$, so that the voltage difference between the two arbitrary terminals would not exceed $2\mathrm{V}_{\mathrm{DDH}}$. The voltages at the nodes Y2, E_{OUT2}, E_{OUT1}, node Z1, and V_{BOT} are approximately $4\mathrm{V}_{\mathrm{DDH}}$, $4\mathrm{V}_{\mathrm{DDH}}$, $4\mathrm{V}_{\mathrm{DDH}} - \mathrm{I}_{\mathrm{CAT}}\mathrm{R}_{\mathrm{S}}$, $2\mathrm{V}_{\mathrm{DDH}} - \mathrm{V}_{\mathrm{TH}}$, and $1\mathrm{V}_{\mathrm{DDH}} - \mathrm{V}_{\mathrm{TH}}$, respectively. Likewise, nodes Y1 and Z2 are about $2\mathrm{V}_{\mathrm{DDH}}$ because M_{PD1} and

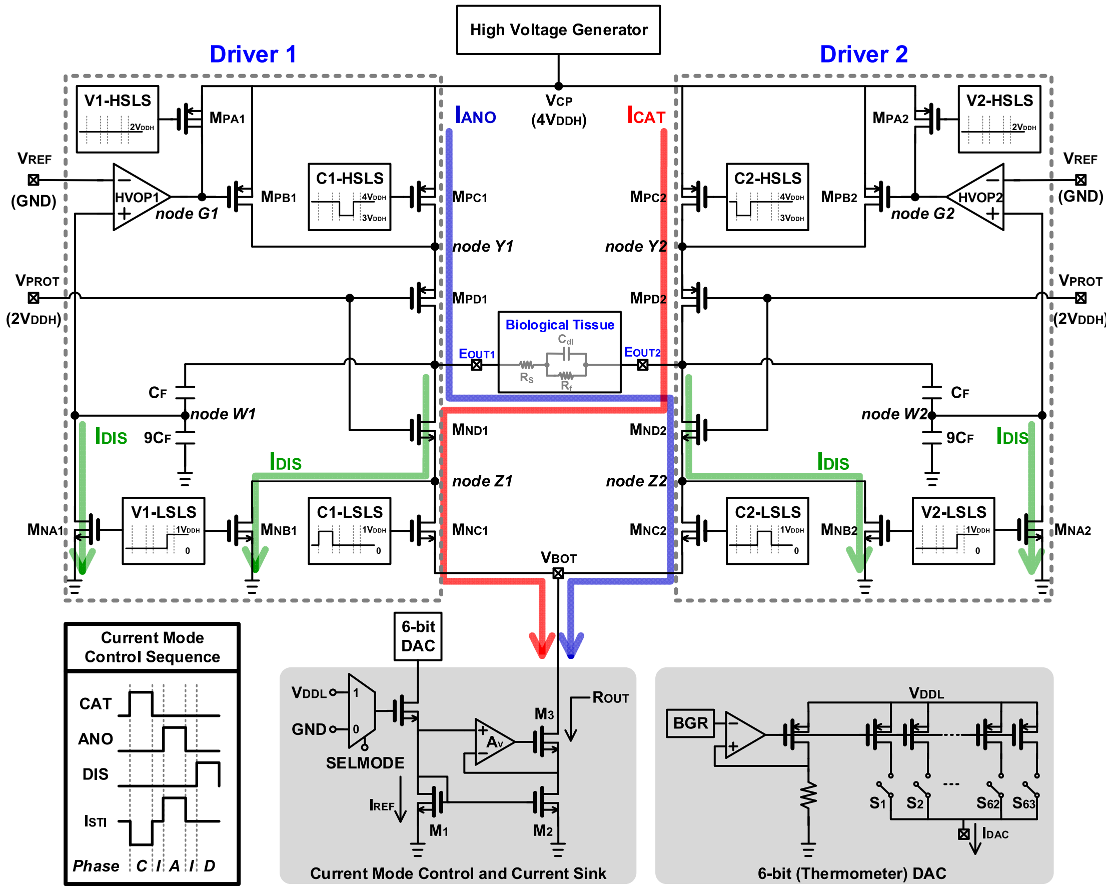

Fig. 4. Detailed circuit architecture and phasic operation for the CCM.

M_{ND2} are turned off. As stated above, each voltage difference is less than $2\mathrm{V}_{\mathrm{DDH}}$. Due to the fixed V_{PROT}, the E_{OUT} nodes are also prevented from the coupling of the switching signal, therefore the tissue would not be influenced during stimulation. In addition, the voltages at the V_{BOT} node vary severely due to the broad stimulus current range. The gain-boosted current mirror with the op-amp was applied for the current sink circuit to adopt this variety. The output impedance (R_{OUT}) can be expressed as:

$$R_{\mathrm{OUT}} \cong g_{m3} r_{02} r_{03} (1 + A_V) \tag{2}$$

where g_{m3} is the transconductance of M_3, r_{O2} and r_{O3} are the output resistance of M_2 and M_3, respectively, and A_V represents the DC gain of the op-amp. The output impedance of a gain-boosted current mirror is more than 10^4 times, while that of a traditional current mirror is only r_{O2}.

An inter-delay time is essential for biphasic stimulus operation. Tissues might be damaged without a delay time between the cathodic and anodic stimulus pulses. Except for M_{PA1} and M_{PA2}, most of the transistors are cut off during the inter-delay phase. In other words, no current path is established on both terminals of the tissue during the inter-delay phase.

In the anodic stimulus phase, the operation is similar to that of the cathodic stimulus phase. But, in reverse, the driver 1 delivers a current stimulus pulse to the driver 2 as an anodic stimulus current (I_{ANO}) on the biological tissue. M_{PC1} and M_{NC2} are entirely conducted. The anodic current sequentially flows through M_{PC1}, M_{PD1}, E_{OUT1}, biological tissue, E_{OUT2}, M_{ND2}, and M_{NC2} (shown with the blue line). Typically, I_{CAT} and I_{ANO} are marked with the same current value but contrary directions. Thus, the biphasic current stimulus pattern can be generated in this system. Similarly, the voltages at nodes Y1, E_{OUT1}, E_{OUT2}, node Z2, and V_{BOT} are approximately $4\mathrm{V}_{\mathrm{DDH}}$, $4\mathrm{V}_{\mathrm{DDH}}$, $4V_{\mathrm{DDH}} - I_{\mathrm{ANO}} R_S$, $2V_{\mathrm{DDH}} - V_{\mathrm{TH}}$, and $1V_{\mathrm{DDH}} - V_{\mathrm{TH}}$, respectively. The proper bias conditions allow the stimulator to avoid the overstress issue on the devices those used in the circuit.

After a short inter-delay phase, the next period of operation will reset the tissue by discharging the electrode nodes to ground. Due to the possible cathodic and anodic current mismatch, some residual charges may be left around the biological tissue. Those residual charges are eliminated and reset to 0 by conducting M_{NA1}, M_{NB1}, M_{NA2}, and M_{NB2} (shown with the green lines).

C. Dual-Mode Stimulus: Voltage Mode Operation

The completed operation and control sequences in the CVM operation are depicted in Fig. 5. In the CVM, the control sequences are classified in three main phases: cathodic stimulus

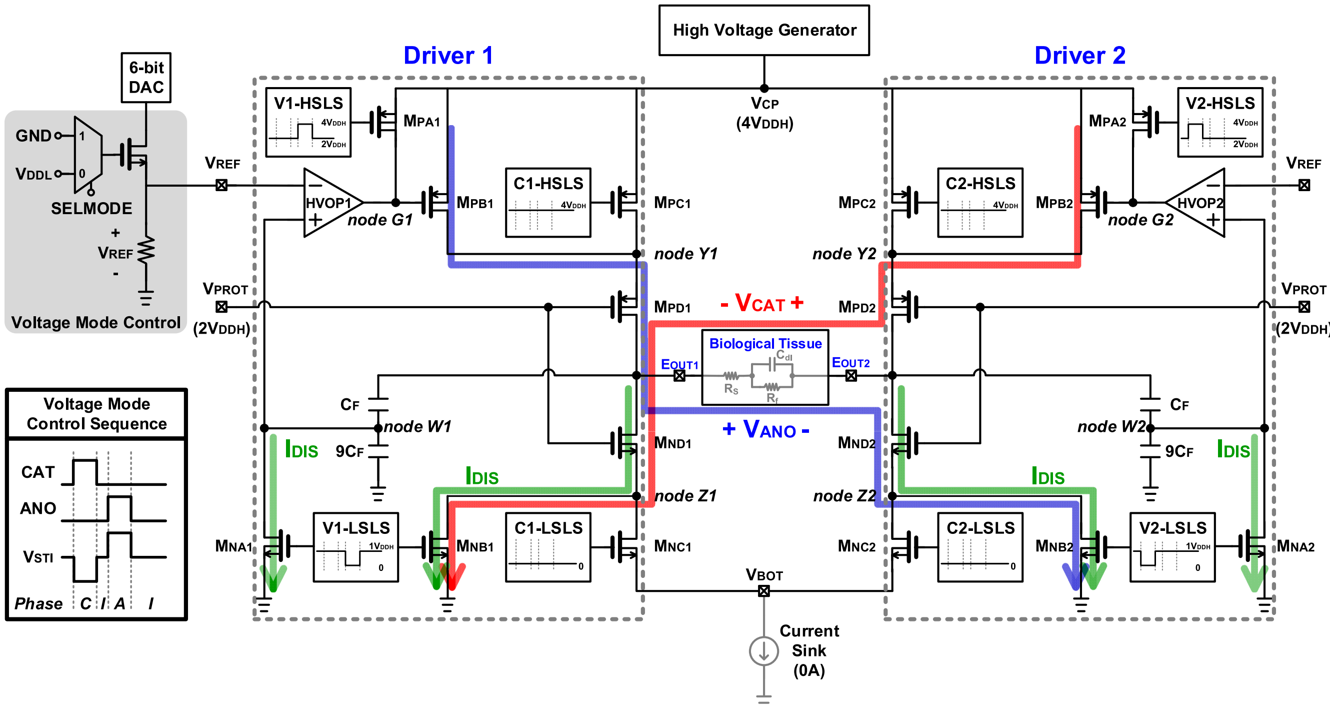

Fig. 5. Detailed circuit architecture and phasic operation for the CVM.

(C), anodic stimulus (A), and inter-delay (I) phases. The discharge phase is merged into the inter-delay (I) phase in the CVM operation. In opposition to the operation of the CCM, the current sink is disabled, but HVOP is enabled in the CVM. The primary switches ($M_{\mathrm{PC1}}, M_{\mathrm{PC2}}, M_{\mathrm{NC1}}$, and M_{NC2}) used in the CCM are turned off to avoid unnecessary current paths in voltage stimulation.

As illustrated in Fig. 5, the cathodic stimulus voltage (V_{CAT}) with constant voltage stimulation is given from driver 2 to driver 1 (shown with the red line). During the cathodic stimulus phase, HVOP1 is asleep, and M_{PB1} is turned off, to keep the upper part of driver 1 at high impedance state. Driver 2 is responsible for generating the stimulation. Thus, HVOP2 drives the output stage with M_{PB2} and a negative feedback loop. Once the feedback loop is built, the node W2 is locked by V_{REF} with a capacitive divider (C_{F} and $9C_{\mathrm{F}}$). Thus, the proposed system can generate different voltage stimulus levels by adjusting V_{REF}. A steady E_{OUT2} is regulated by this loop, and the desired stimulus voltage is delivered to the tissue. The voltage at E_{OUT1} node is near 0V due to the fully turned-on M_{ND1} and M_{NB1}. Therefore, a voltage difference across the biological tissue is established as V_{CAT}.

Additionally, Fig. 6 shows the configuration of HVOP. The overall closed-loop gain A_{VM} in the CVM can be expressed as

$$A_{VM} \cong A_{HVOP} \cdot g_{mPB2} \left[(g_{mPD2} r_{OPB2} r_{OPD2}) \| R_{eq} \right] \times \frac{C_F}{C_F + 9C_F} \tag{3}$$

where A_{HVOP} represents the DC gain of HVOP. The g_{mPB2}, g_{mPD2}, r_{OPB2}, and r_{OPD2} are the transconductance and output resistance of M_{PB2} and M_{PD2}, respectively. R_{eq} denotes the resistive part of the tissue model in series with a triode-region resistance of M_{ND1} and M_{NB1}. Typically, A_{VM} can reach about 60 dB to 80 dB, so the voltage error between the two input terminals of HVOP will be tiny. For the aforementioned overstress concern, any two terminals in the circuit operations are designed within the voltage range of $2 \times V_{\mathrm{DDH}}$. The voltage of node Y2 is at the flexible analog level (between $2V_{\mathrm{DDH}}$ and $4V_{\mathrm{DDH}}$), the voltage at E_{OUT2} is $10V_{\mathrm{REF}}$ (lower than $2V_{\mathrm{DDH}}$), and the voltages at nodes E_{OUT1} and Z1 are near 0V.

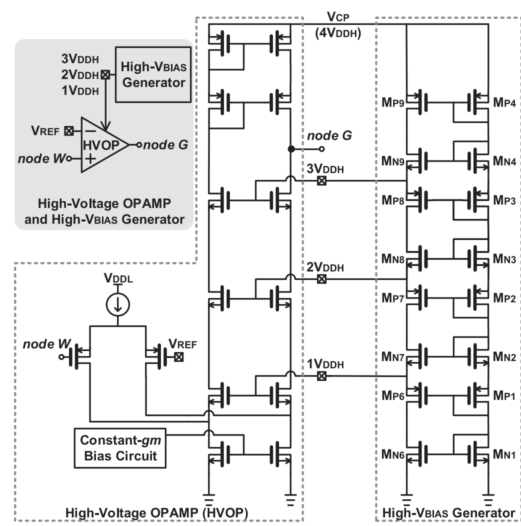

Fig. 6. Detailed circuit schematic for the high-voltage op-amp (HVOP) and high-V_{BIAS} generator.

Unlike the CCM stimulus, the inter-delay phase of the CVM also plays a role in dismissing the residual charges. During this

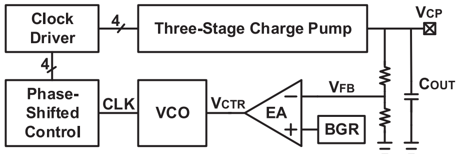

Fig. 7. Block diagram of the high-voltage generator (charge pump).

inter-delay phase, all of HVOP are shut down, but $M_{\rm NA1}$, $M_{\rm NB1}$, $M_{\rm NA2}$, and $M_{\rm NB2}$ are fully turned on, therefore the charges remaining on the tissue can be discharged directly (shown with the green lines).

During the anodic stimulus phase, the reverse voltage stimulation on the biological tissue is driven from driver 1 to driver 2 (shown with the blue line). The operation is similar, but the current direction is opposite. HVOP1, $M_{\rm PB1,}$ and $M_{\rm PD1}$ are charged to deliver an anodic stimulus voltage ($V_{\rm ANO}$) on the tissue. Hence, $M_{\rm ND2}$ and $M_{\rm NB2}$ are fully turned on to form a stimulation path in the lower part of driver 2. Meanwhile, the voltage difference across the biological tissue is $V_{\rm ANO}$. Finally, the CVM operation goes back to the inter-delay phase. Most nodes are reset, and the drivers return to the original state. $V_{\rm CAT}$ and $V_{\rm ANO}$ are provided with the same voltage value but opposite polarity. Thus, the biphasic voltage stimulus pattern can be generated in this system.

D. High Voltage Generator

Fig. 7 is a block diagram of the high voltage generator realized with three-stage charge pump circuit. The charge pump was used to create the highest voltage supply of 4 $\times$ $V_{\rm DDH}$ in this work. Because the current stimulus range is extensive, the high voltage generator must be able to withstand the current loading for stimulus and still to maintain the desired power voltage level. The pulse frequency modulation (PFM) technique was applied. Once the load current increases, the operation frequency of the charge pump will be raised. Therefore, the output voltage ($V_{\rm CP}$) can maintain its level even under heavy current loading. An analog voltage ($V_{\rm CTRL}$) is given by PFM feedback to the voltage-controlled oscillator (VCO). Consequently, the system clock (CLK) becomes faster and causes the output voltage to increase. Therefore, the output voltage can maintain a range by using the feedback control. For implantable biomedical applications, the efficiency and reliability of the charge pump is significant. Thus, the cross-coupled structure is used in the pump circuit to avoid neither the dropout of the threshold voltage nor the over-stress problem [33]. In addition, a phase-shifted clock control is designed to generate four non-overlap phase clocks, which are used to further reduce the return-back leakage current [34].

III. Silicon Verifications and Animal Experiments

The proposed dual-mode stimulus chip has been fabricated in tsmc 0.25-μm 2.5V/5V/12V CMOS process, and the die microphotograph is shown in Fig. 8. The entire chip area is 3.85 mm^2. The high voltage generator occupies a silicon area of 1.64 mm^2, and the common-shared circuits (bias circuit, DAC, and operation mode control) occupy a silicon area of 1.33 mm^2. Thus, the 4-channel driver without the shared part is only 0.88 mm^2, and the silicon area per channel is about 0.22 mm^2. When adding more channels, each additional area per channel is 0.22 mm^2. The required area per channel is also important, when the stimulus channels are extended for more compenhansive applications.

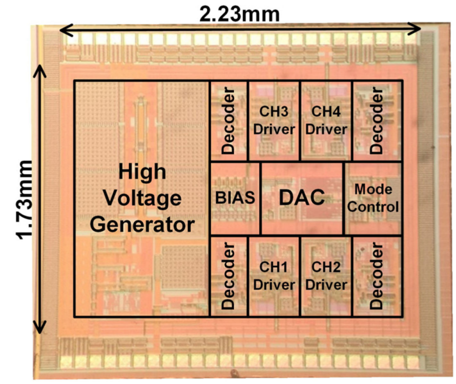

Fig. 8. Die microphotograph of the dual-mode stimulus chip, all of the sub-circuit blocks are also marked.

A. Silicon Verifications

The current stimulus results in the CCM operation are shown in Fig. 9(a). To verify the CCM, AMP [6:1] was set to logic 110010 for generating the target maximum stimulus current of 5 mA. In Fig. 9(a), the cathodic signal (CAT) elicited a desired neural response, and the anodic signal (ANO) is used to achieve charge balance. A stimulus current was produced in the cathodic phase, followed by the inter-delay, and then the anodic phase. The stimulus pulse width (both CAT and ANO) was set as 50 μs, and the tissue took a rest within an inter-delay time of 10 μs. In addition, the tissue load for verifications is set with R_s, C_{dl}, and R_f of 3 kΩ, 150 nF, and 1 MΩ, respectively. First of all, the high voltage generator verified in the silicon was able to provide a high supply voltage of 17.8 V for CCM and CVM operations. Due to the mechanism of PFM, the output ripples of $V_{\rm CP}$ in the cathodic and anodic stimulus phases were found to be smaller than that in the inter-delay phase. Overall, the stimulator was able to produce the stimulus currents of –5.02 mA ($I_{\rm CAT}$) and +5.01 mA ($I_{\rm ANO}$) in the CCM. In this work, the fabricated silicon chip was able to output the stimulus current from 0.1 mA to 5 mA (0.1 mA per step). Fig. 9(b) shows the specified current stimulus results, such as 1 mA, 2 mA, 3 mA, 4 mA, and 5 mA, respectively. The CCM stimulus with a built-in high voltage generator was successfully proven to be functional and stable with the maximum stimulus current of up to 5 mA.

In the CVM operation, AMP [6:1] was set to logic 010100 for generating the target maximum stimulus voltage of 10 V. The corresponding voltage stimulus waveforms are shown in Fig. 10(a). The control operations, regarding CAT and ANO signals, are the same as those in the CCM. The stimulator

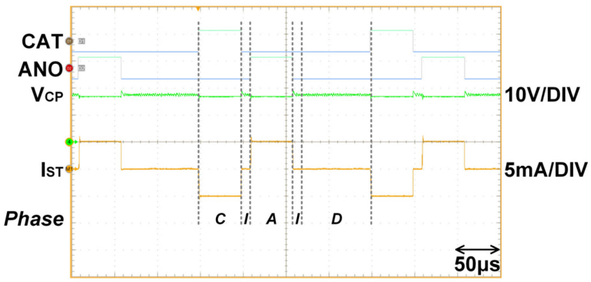

(a)

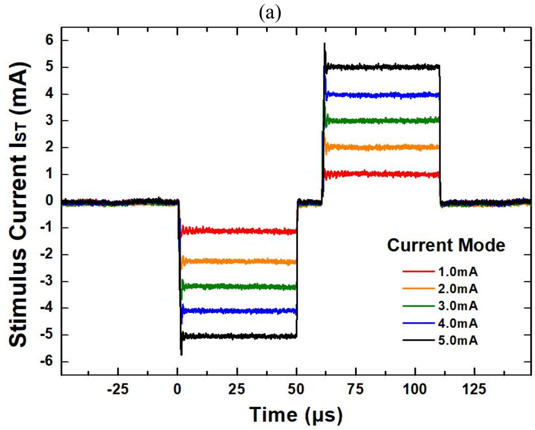

(b)

Fig. 9. Measurement results of the CCM operation with built-in high voltage generator and the R_s, C_{dl}, and R_f of tissue load are set as 3 kΩ, 150 nF, and 1 MΩ, respectively. (a) 5 mA in CCM. (b) 1 mA, 2 mA, 3 mA, 4 mA, and 5 mA in CCM.

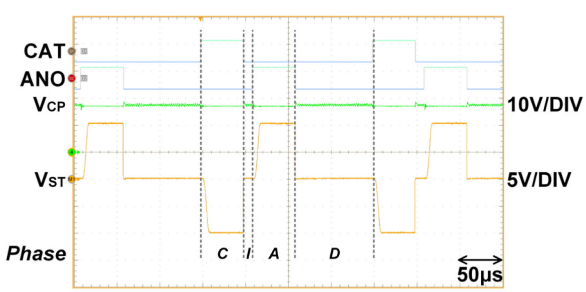

(a)

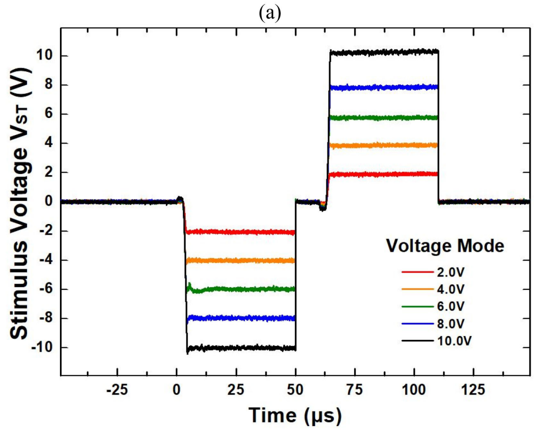

(b)

Fig. 10. Measurement results of the CVM operation with built-in high voltage generator and the R_s, C_{dl}, and R_f of tissue load are set as 3 kΩ, 150 nF, and 1 MΩ, respectively. (a) 10 V in CVM. (b) 2 V, 4 V, 6 V, 8 V, and 10 V in CVM.

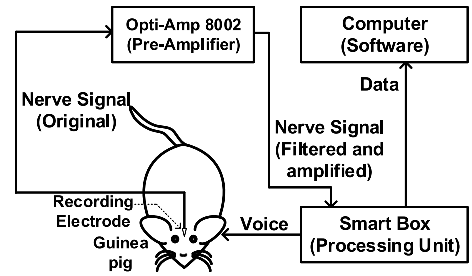

(a)

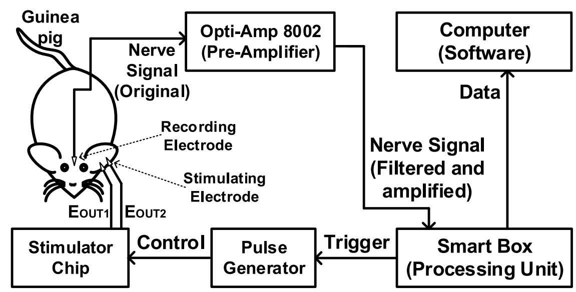

(b)

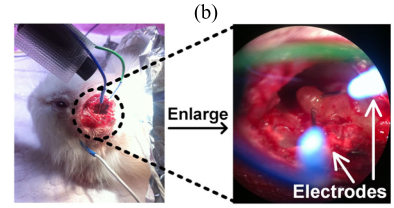

(c)

Fig. 11. (a) Animal experimental setup for the conventional auditory brainstem response (ABR) measurement. (b) Experimental setup for the electrically elicited auditory brainstem response (ee-ABR) measurement. (c) Enlarged photo of a guinea pig's middle ear with the implanted electrodes.

was able to produce the stimulus voltages of –10.05 V (V_{CAT}) and +10.06 V (V_{ANO}) in the CVM. Through the measurement results, the fabricated silicon chip was demonstrated to generate the maximum stimulus voltage up to 10 V. In the CVM, the proposed system was able to output the stimulus voltage from 0.5 V to 10 V (0.5 V per step). Fig. 10(b) presents the specified voltage stimulus results with the voltage levels of 2 V, 4 V, 6 V, 8 V, and 10 V. In conclusion, the proposed dual-mode stimulus system was successfully verified in the fabricated silicon chip.

B. In-Vitro Animal Experiments

The proposed dual-mode stimulus function was verified via the *in-vitro* animal experiment. The animal experiment analyzed the neural responses in guinea pigs through the auditory brainstem response (ABR) plot. The ABR is a technique that stimulates the peripheral hearing nerves with sound to induce a lot of nerve discharges before recording the nerve change potentials [35], [36]. The data acquired by ABR usually consists of six to seven peak waves. Furthermore, the waves I to V normally occur within the first 10 ms after the stimulation sequence, which are evaluated more often in the medical field. Generally speaking, different peak waves are caused by different auditory structures. For instance, the source of wave V may come from the upper brain stem. Fig. 11(a) illustrates the experimental setup for the

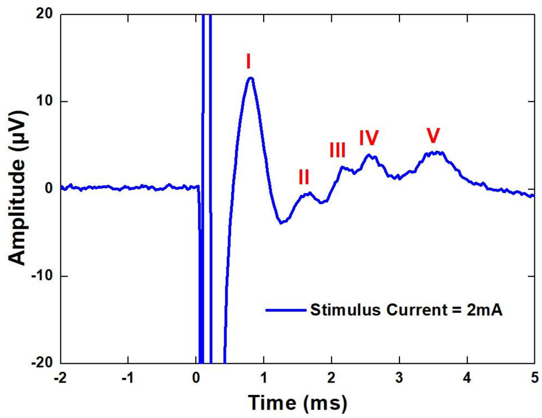

(a)

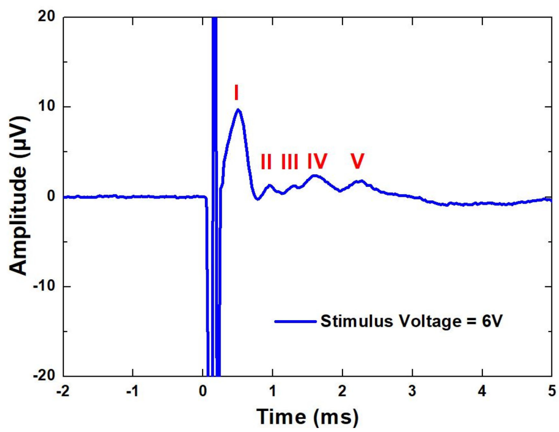

(b)

Fig. 12. Measured ABR waveform results in the animal experiments. (a) 2 mA in CCM. (b) 6 V in CVM.

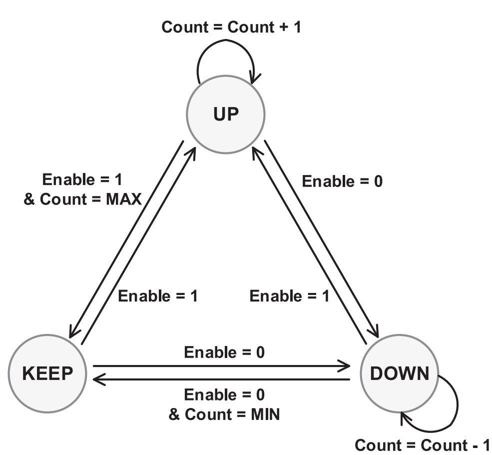

Fig. 13. Finite state machine (FSM) plot for the digital controller.

conventional ABR measurement in more detail. The software program in the computer used in the experiment will judge whether the stimulus is successful, or not.

The SmartEP box (processing unit) and the Opti-Amp 8002 pre-amplifier (Intelligent Hearing Systems company, IHS) were used. First, the processing unit plays a sound to the subject to cause a nervous reaction. The wave passes through the recording electrode and amplifier back to the processing unit to perform

TABLE I
STATE DESCRIPTIONS FOR DIGITAL CONTROLLER

State/Trigger	Action
KEEP	Maintain the current state and do nothing.
UP	Keep increasing AMP [6:1] by one.
DWON	Keep decreasing AMP [6:1] by one.
+1	Increase AMP [6:1] by one through the counter.
-1	Decrease AMP [6:1] by one through the counter.
Enable=1/0	The state would change to UP/DOWN.
Count=MAX/MIN	The counter reaches the upper/lower limit.

signal processing. Eventually, the software program performs the calculation and outputs the required ABR plots.

To verify the stimulator chip, the experimental setup was slightly modified. The voice trigger was changed to electrical stimulation signals through the function generator, and the stimulus chip is used to produce the corresponding neural responses by applying the stimulus current or voltage to the hearing nerves through the implanted electrodes. This electrical triggering method is called as electrically elicited auditory brainstem responses (ee-ABR), and the experimental settings for measurement are shown in Fig. 11(b). Similarly, the neural signals can be also converted to the ABR plot through the commercial hardware and software in the computer.

The experimental photo on the guinea pig's middle ear with the implanted electrodes is shown in Fig. 11(c). In this animal test, the stimulus current and voltage levels were set to 2 mA and 6 V, respectively. The values of R_s, C_{dl}, *and* R_f were measured as 5 kΩ, 80 nF, and 6 MΩ, respectively. Therefore, the maximum equivalent current formed in the CVM was about 6 V/5 kΩ = 1.2 mA, which is lower than the current of 2 mA set in the CCM. Based on the viewpoint of total charges in stimulus, the stimulation effects of the CVM should be weaker than that of the current one.

The measured waveforms of current and voltage stimulus with the assistance of the ABR system are shown in Fig. 12(a) and Fig. 12(b), respectively. The wave I to wave V can be clearly observed in both pictures. Furthermore, it can be observed from the figures that the response of voltage stimulation is smaller than that of the current stimulation. However, these two stimulation modes were judged as successful by the ABR system. From animal experiment, the result illustrates that the dual-mode stimulus chip works successfully not only in the silicon but also in the practical biomedical experiments.

C. Other Applications

For some biomedical applications, such as the treatment of Parkinson's disease, the climbing stimulus waveform was requested [37]. When abnormal nerve electricity was detected, a control signal was sent, and the stimulus waveform climbed slowly. With a mild rising stimulus waveform, the patient would

TABLE II
PERFORMANCE COMPARISON WITH RELATED PRIOR WORKS

	Z. Luo [28] (TBioCAS 2017)	**M. Haas [15] (SSC-L 2018)**	**D. Jiang [14] (TBioCAS 2018)**	**N. Butz [22] (JSSC 2018)**	**A. Urso [25] (TBioCAS 2019)**	**This work**
Technology	0.18-μm CMOS	0.18-μm CMOS	0.6-μm CMOS	0.35-μm CMOS	0.18-μm CMOS	**0.25-μm CMOS**
Supply Voltage	1.8 V/ 3.3 V	± 9 V	5 V/ 12 V	3 V/ 22 V	3.5 V	**2.5 V/5 V**
Stimulus Mode	CCM	CCM/CVM	Chopped CCM	CCM	*UFH CM	**CCM/CVM**
Stimulus Current	0 ~ 3 mA	0 ~ 10.2 mA	0 ~1 mA	0 ~ 5 mA	0 ~ 10 mA	**0 ~ 5 mA**
Stimulus Voltage	N/A	± 6 V	N/A	N/A	N/A	**0 ~ 10 V**
Load Condition (R_s / C_{dl})	1 kΩ / 100 nF	N/A	2 kΩ / 100 nF	1 kΩ / 100 nF	1 kΩ / 500 nF	**3 kΩ / 150 nF**
High Voltage Generator	Yes	No	No	No	Yes	**Yes**
Off-Chip Components	No	N/A	No	No	Yes	**No**
Number of Channels	16	1	2	1	8	**4**
Area Per Channel	0.1 mm^2	0.24 mm^2	0.5 mm^2	1.24 mm^2	0.23 mm^2	**0.22 mm^2**

*UFH CM represents the ultra-high frequency current mode and realized through DC-DC converter.

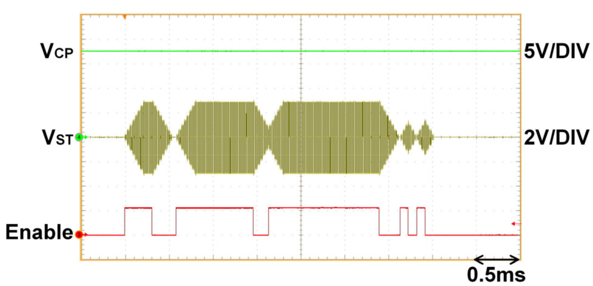

Fig. 14. Measurement results of the climbing stimulus voltage waveform.

not suffer from sudden and excessive stimulation. A digital controller was used to control the ANO and CAT signals and the amplitude signal AMP [6:1] of the proposed dual-mode stimulus chip to achieve the requested function. Fig. 13 shows the finite state machine (FSM) plot of the digital controller. In the beginning, AMP [6:1] was set to 000000. The initial state of the digital controller was "KEEP," which would maintain the current state and do nothing. Once the "enable" signal was turned to high, the state was then changed to "UP." Then, the counter in the digital controller started to count and increase the AMP [6:1]. When the enable signal becomes low or the counter reaches the upper limit, the state can be changed again. A more detailed explanation of the FSM states and the corresponding actions are described in Table I.

Consequently, the results of the climbing stimulus waveform are measured and exhibited in Fig. 14. As the enable signal goes high state with the supply voltage V_{CP} of 17.8 V, the dual-mode stimulus system starts to output the biphasic voltage stimulus pulses. The maximum voltage value for this experiment was set at 3 V. When the output voltage (V_{ST}) reaches 3 V, the digital controller is in the "KEEP" state, and then waits for the next control signal to convert its state. When the enable signal is high longer in time, the higher voltage stimulus level is generated. This experiment exhibited the high flexibility and reliability of the proposed dual-mode stimulus system for wide biomedical applications.

IV. CONCLUSIONS

In biomedical applications, neuromodulation by electrical current or voltage stimulus has been widely used to treat neurological disorders. A dual-mode stimulus system is proposed to generate the biphasic current or voltage stimulation for biomedical applications, which has been successfully verified in a 0.25-μm 2.5V/5V/12V CMOS process. The stimulus system only requires an area of 0.22 mm^2 per single channel, and the built-in high voltage generator was also fully on-chip integrated without additional external components. Performance comparisons to prior works are shown in Table II. This work has been practically verified with *in-vitro* animal experiments. With the features of dual-mode operation, flexibility, and reliability, the proposed stimulator is very suitable for being integrated with analog frond-end circuits and bio-signal processor together via the SoC technology for most biomedical applications.

REFERENCES

[1] X.-H. Qian *et al.*, "A bone-guided cochlear implant CMOS microsystem preserving acoustic hearing," in *Proc. Symp. VLSI Circuits. Dig. Tech. Papers*, 2017, pp. C46–C47.
[2] V. Valente, A. Demosthenous, and R. Bayford, "A tripolar current-steering stimulator ASIC for field shaping in deep brain stimulation," *IEEE Trans. Biomed. Circuits Syst.*, vol. 6, no. 3, pp. 197–207, May 2012.
[3] Y. P. Lin *et al.*, "A battery-less, implantable neuro-electronic interface for studying the mechanisms of deep brain stimulation in rat models," *IEEE Trans. Biomed. Circuits Syst.*, vol. 10, no. 1, pp. 98–112, Feb. 2016.
[4] H.-M. Lee, H. Park, and M. Ghovanloo, "A power-efficient wireless system with adaptive supply control for deep brain stimulation," *IEEE J. Solid-State Circuits*, vol. 48, no. 9, pp. 2203–2216, Sep. 2012.
[5] H.-M. Lee, K. Y. Kwon, W. Li, and M. Ghovanloo, "A power-efficient switched-capacitor stimulating system for electrical/optical deep brain stimulation," *IEEE J. Solid-State Circuits*, vol. 50, no. 1, pp. 360–374, Jan. 2015.

[6] Y.-K. Lo *et al.*, "A fully integrated wireless SoC for motor function recovery after spinal cord injury," *IEEE Trans. Biomed. Circuits Syst.*, vol. 11, no. 3, pp. 497–509, Jun. 2017.
[7] J. S Q. Xu, D. Hu, B. Duan, and J. He, "A fully implantable stimulator with wireless power and data transmission for experimental investigation of epidural spinal cord stimulation," *IEEE Trans. Neural Syst. Rehabil. Eng.*, vol. 23, no. 4, pp. 683–92, Jul. 2015.
[8] L. S. Theogarajan, "A low-power fully implantable 15-channel retinal stimulator chip," *IEEE J. Solid-State Circuits*, vol. 43, no. 10, pp. 2322–2337, Oct. 2008.
[9] Y. K. Lo, K. Chen, P. Gad, and W. Liu, "A fully-integrated high-compliance voltage SoC for epi-retinal and neural prostheses," *IEEE Trans. Biomed. Circuits Syst.*, vol. 7, no. 6, pp. 761–772, Dec. 2013.
[10] M. Ortmanns, A. Rocke, M. Gehrke, and H.-J. Tiedtke, "A 232-channel epiretinal stimulator ASIC," *IEEE J. Solid-State Circuits*, vol. 42, no. 12, pp. 2946–2959, Dec. 2007.
[11] C.-H. Cheng *et al.*, "A fully integrated 16-channel closed-loop neural-prosthetic CMOS SoC with wireless power and bidirectional data telemetry for real-time efficient human epileptic seizure control," *IEEE J. Solid-State Circuits*, vol. 53, no. 11, pp. 232–247, Sep. 2018.
[12] M. T. Salam, J. L. P. Velazquez, and R. Genov, "Seizure suppression efficacy of closed-loop versus open-loop deep brain stimulation in a rodent model of epilepsy," *IEEE Trans. Neural Syst. Rehabil. Eng.*, vol. 24, no. 6, pp. 710–719, Jun. 2016.
[13] C.-Y. Wu, C.-H. Cheng, and Z.-X. Chen, "A 16-channel CMOS chopper-stabilized analog front-end ECoG acquisition circuit for a closed-loop epileptic seizure control system," *IEEE Trans. Biomed. Circuits Syst.*, vol. 12, no. 3, pp. 543–553, Jun. 2018.
[14] D. Jiang and A. Demosthenous, "A multichannel high-frequency power-isolated neural stimulator with crosstalk reduction," *IEEE Trans. Biomed. Circuits Syst.*, vol. 12, no. 4, pp. 940–953, May 2018.
[15] M. Haas, P. Vogelmann, and M. Ortmanns, "A neuromodulator frontend with reconfigurable class-b current and voltage controlled stimulator," *IEEE Solid-State Circuits Lett.*, vol. 1, no. 3, pp. 54–57, Mar. 2018.
[16] D. R. Merrill, M. Bikson, and G. R. Jefferys, "Electrical stimulation of excitable tissue: Design of efficacious and safe protocols," *J. Neurosci.Methods*, vol. 141, no. 2, pp. 171–198, Feb. 2005.
[17] S. Venkatraman *et al.*, "In vitro and in vivo evaluation of PEDOT microelectrodes for neural stimulation and recording," *IEEE Trans. Neural Syst. Rehabil. Eng.*, vol. 19, no. 3, pp. 307–316, Jun. 2011.
[18] V. S. Polikov, P. A. Tresco, and W. M. Reichert, "Response of brain tissue to chronically implanted neural electrodes," *J. Neurosci. Methods*, vol. 148, no. 1, pp. 1–18, Oct. 2005.
[19] Z. Luo and M.-D. Ker, "A high-voltage-tolerant and power-efficient stimulator with adaptive power supply realized in low-voltage CMOS process for implantable biomedical applications," *IEEE J. Emerg. Sel. Top. Circuits Syst.*, vol. 8, no. 2, pp. 178–186, Jun. 2018.
[20] M.-D. Ker, C. Y. Lin, and W. L. Chen, "Stimulus driver for epilepsy seizure suppression with adaptive loading impedance," *J. Neural Eng.*, vol. 8, no. 6, Dec. 2011.
[21] H. Chun, Y. Yang, and T. Lehmann, "Safety ensuring retinal prosthesis with precise charge balance and low power consumption," *IEEE Trans. Biomed. Circuits Syst.*, vol. 8, no. 1, pp. 108–118, May 2013.
[22] N. Butz, A. Taschwer, S. Nessler, Y. Manoli, and M. Kuhl, "A 22 V compliant 56 μW twin-track active charge balancing enabling 100% charge compensation even in monophasic and 36% amplitude correction in biphasic neural stimulators," *IEEE J. Solid-State Circuits*, vol. 53, no. 8, pp. 2298–2310, Aug. 2018.
[23] Z. Luo and M.-D. Ker, "A high-voltage-tolerant and precise charge-balanced neuro-stimulator in low voltage CMOS process," *IEEE Trans. Biomed. Circuits Syst.*, vol. 10, no. 6, pp. 1087–1099, Dec. 2016.
[24] S. Luan, T. G. Constandinou, "A novel charge-metering method for voltage mode neural stimulation," in *Proc. IEEE Int. Symp. Circuits Syst.*, 2012, pp. 2239–2242.
[25] A. Urso, V. Giagka, M. van Dongen, and W. A. Serdijn, "An ultra high-frequency 8-channel neurostimulator circuit with 68% peak power efficiency," *IEEE Trans. Biomed. Circuits Syst.*, vol. 13, no. 3, pp. 882–892, Oct. 2019.
[26] J. Simpson and M. Ghovanloo, "An experimental study of voltage, current, and charge controlled stimulation front-end circuitry," in *Proc. IEEE Int. Symp. Circuits Syst.*, 2007, pp. 325–328.
[27] W. Y. Hsu and A. Schmid, "Compact, energy-efficient high-frequency switched capacitor neural stimulator with active charge balancing," *IEEE Trans. Biomed. Circuits Syst.*, vol. 11, no. 4, pp. 878–888, Aug. 2017.
[28] Z. Luo, M.-D. Ker, T.-Y. Yang, and W.-H. Cheng, "A digitally dynamic power supply technique for 16-channel 12V-tolerant stimulator realized in a 0.18-μm 1.8-V/3.3-V low-voltage CMOS process," *IEEE Trans. Biomed. Circuits Syst.*, vol. 11, no. 5, pp. 1087–1096, Jul. 2017.
[29] E. Noorsal, K. Sooksood, H. Xu, R. Hornig, J. Becker, and M. Ortmanns, "A neural stimulator frontend with high-voltage compliance and programmable pulse shape for epiretinal implants," *IEEE J. Solid-State Circuits*, vol. 47, no. 1, pp. 244–256, Jan. 2012.
[30] S. Washburn, R. Catlin, K. Bethel, and B. Canlas, "Patient-perceived differences between constant current and constant voltage spinal cord stimulation systems," *Neuromodulation*, vol. 17, no. 1, pp. 28–35, Jan. 2014.
[31] S. K. Arfin and R. Sarpeshkar, "An energy-efficient, adiabatic electrode stimulator with inductive energy recycling and feedback current regulation," *IEEE Trans. Biomed. Circuits Syst.*, vol. 6, no. 1, pp. 1–14, Feb. 2012.
[32] M. van Dongen and W. Serdijn, "A power-efficient multichannel neural stimulator using high-frequency pulsed excitation from an unfiltered dynamic supply," *IEEE Trans. Biomed. Circuits Syst.*, vol. 10, no. 1, pp. 61–71, Feb. 2016.
[33] Y-H. Weng, H.-W. Tsai, and M.-D. Ker, "Design of charge pump circuit in low-voltage CMOS process with suppressed return-back leakage current," in *Proc. IEEE Int. Conf. Integr. Cir. Des. Technol.*, 2010, pp. 155–158.
[34] Y.-H. Weng, H.-W. Tsai, and M.-D. Ker, "Design to suppress return-back leakage current of charge pump circuit in low-voltage CMOS process," *Microelectron. Rel.*, vol. 51, no. 5, pp. 871–878, May 2011.
[35] S. Gallego, E. Truy, A. Morgon, and L. Collet, "EABRs and surface potentials with a transcutaneous multielectrode cochlear implant," *Acta Otolaryngologica*, vol. 117, no. 2, pp. 164–168, Mar. 1997.
[36] X.-H. Qian *et al.* "Design and in-vivo verification of a CMOS bone-guided cochlear implant microsystem," *IEEE Trans. Biomed. Eng.*, vol. 66, no. 11, pp. 3156–3167, Nov. 2019.
[37] S. Little *et al.*, "Adaptive deep brain stimulation in advanced parkinson disease," *Ann. Neurol.*, vol. 74, pp. 449–457, Sep. 2013.

Ting-Yang Yen received the B.S. degree in electronics engineering from National Sun Yat-sen University, Kaohsiung, Taiwan, in 2014, and the M.S. degree from the Institute of Electronics, National Chiao-Tung University, Hsinchu, Taiwan, in 2016. He is currently with the eMemory Technology, Inc., Hsinchu, Taiwan, engaging with the design of analog and mixed-signal integrated circuits for non-volatile memory applications.

Ming-Dou Ker (Fellow, IEEE) received the Ph. D. degree from the Institute of Electronics, National Chiao-Tung University (NCTU), Hsinchu, Taiwan, in 1993.

He is currently the Distinguished Professor with the Institute of Electronics, NCTU, and also the Director of Biomedical Electronics Translational Research Center, NCTU, working on biomedical electronics translational projects. In the technical field of reliability and quality design for microelectronic circuits and systems, he has authored or co-authored more than 570 technical papers in international journals and conferences. He has proposed many useful solutions to improve the reliability and quality of integrated circuits, which have been granted with hundreds of U.S. patents. His current research interests include the circuits and systems for biomedical applications, as well as circuit-related reliability issue.

Prof. Ker has served as a member of the Technical Program Committee and the Session Chair of numerous international conferences for many years, including the IEEE Symposium on VLSI Circuits, IEEE International Symposium on Circuits and Systems (ISCAS), and IEEE International Solid-State Circuits Conference (ISSCC). He served as Associate Editor for the IEEE TRANSACTIONS ON VLSI SYSTEMS, IEEE TRANSACTIONS ON BIOMEDICAL CIRCUITS AND SYSTEMS (TBioCAS), and the Guest Editor for *ISCAS2019 Special Issue in TBioCAS*. He is currently the Editor for the IEEE TRANSACTIONS ON DEVICE AND MATERIALS RELIABILITY.